

Energy transfer mechanisms in a dipole chain: From energy equipartition to the formation of breathers

Alexandra Zampetaki,¹ J. Pablo Salas,² and Peter Schmelcher^{1,3}

¹*Zentrum für Optische Quantentechnologien, Universität Hamburg, Luruper Chaussee 149, 22761 Hamburg, Germany*

²*Área de Física, Universidad de La Rioja, 26006 Logroño, La Rioja, Spain*

³*The Hamburg Center for Ultrafast Imaging, Luruper Chaussee 149, 22761 Hamburg, Germany*



(Received 14 March 2018; published 6 August 2018)

We study the energy transfer in a classical dipole chain of N interacting rigid rotating dipoles. The underlying high-dimensional potential energy landscape is analyzed in particular by determining the equilibrium points and their stability in the common plane of rotation. Starting from the minimal energy configuration, the response of the chain to excitation of a single dipole is investigated. Using both the linearized and the exact Hamiltonian of the dipole chain, we detect an approximate excitation energy threshold between a weakly and a strongly nonlinear dynamics. In the weakly nonlinear regime, the chain approaches in the course of time the expected energy equipartition among the dipoles. For excitations of higher energy, strongly localized excitations appear whose trajectories in time are either periodic or irregular, relating to the well-known discrete or chaotic breathers, respectively. The phenomenon of spontaneous formation of domains of opposite polarization and phase locking is found to commonly accompany the time evolution of the chaotic breathers. Finally, the sensitivity of the dipole chain dynamics to the initial conditions is studied as a function of the initial excitation energy by computing a fast chaos indicator. The results of this study confirm the aforementioned approximate threshold value for the initial excitation energy, below which the dynamics of the dipole chain is regular and above which it is chaotic.

DOI: [10.1103/PhysRevE.98.022202](https://doi.org/10.1103/PhysRevE.98.022202)

I. INTRODUCTION

The first numerical study of the energy transport in a one-dimensional (1D) nonlinear oscillator chain, known as the Fermi-Pasta-Ulam (FPU) model [1–3] has been performed already in 1955. The results of this numerical experiment were found to contradict the reasonable assumption that in the presence of a nonlinear coupling between the oscillators the system would thermalize, i.e., an initial excitation of a single mode of the system would become equally distributed between all the modes of the chain. In particular, the numerical results showed a persistent recurrence of the energy to the initially excited mode, preventing the system from reaching equipartition up to long times. It has been soon realized that the origin of such a behavior were the nonlinear interaction terms, a fact that established the study of the energy exchange in discrete nonlinear lattices of oscillators as an active field of research in few- and many-body dynamics; see, for instance, Refs. [2,4–10]. Most attention has been paid to 1D oscillator chains with a cubic or quartic nonlinear coupling, the so-called FPU- α and FPU- β models, respectively, [2]. Already studies of the energy transfer in these simple FPU models have provided interesting results, such as the existence of thresholds for stochasticity and therefore for equipartition [10–12], as well as the discovery of phenomena of energy localization in discrete [13–15] or chaotic breathers [15–17].

Beyond the theoretical FPU-like models, the mechanism of energy exchange is an important subject of investigation in microscopic systems such as molecules, interacting via Coulomb, dipole-dipole or van der Waals interactions. These fundamental interactions appear in different research

disciplines including physics, chemistry, biology and material sciences, with applications covering such diverse topics as the photosynthesis of plants and bacteria [18–22], the emission of light of organic materials [23–25], molecular crystals [26–28], or artificial molecular rotors [29]. Moreover the advances in current technology have allowed the trapping and confinement of cold molecules in optical lattices where the positions of the molecules are fixed and their mutual interactions (e.g., dipole-dipole) usually masked by thermal fluctuation, become prominent [30,31]. Along these lines polar diatomic molecules trapped in optical lattices, exhibit due to their strong dipole-dipole interaction a particularly interesting quantum many-body behavior leading to novel structures and collective dynamics [32–34].

Within the framework of classical mechanics, confined polar diatomic molecules can be considered as lattices of rigid dipoles. Following this approach, Ratner and coworkers [35–37] have studied the energy transfer in chains of interacting rotating rigid dipoles in various planar configurations. Already the simplest two-dipole chain, recently revisited in Ref. [38], was found to display a rich dynamical behavior with a complicated phase space. Increasing the number of dipoles the energy transfer was shown to yield the formation of solitons or the emergence of chaoticity [39].

The objective of this paper is to provide further insights in the energy transfer mechanisms of a 1D chain of rotating classical dipoles. In such a chain the dipoles are assumed to be fixed in space, interacting through nearest neighbor (NN) interactions and rotating in a common plane. The interaction potential of even this simplified rigid-rotor model is found to be quite complex, supporting various equilibrium points

including a minimum, a maximum and different saddle points. Considering the system in its ground state (GS) configuration (minimum) with a single dipole excited initially possessing a certain amount of kinetic energy we study the transport of the excess energy. We find that for increasing excess energy the degree of chaoticity of the energy transfer increases, passing through a weakly nonlinear and a highly nonlinear regime. Although in the former regime after some time the energy is almost equally partitioned among the dipoles of the chain, for high enough excitation energies the energy diffusion is prohibited, giving place to different energy localization patterns dictated by a strong nonlinearity. Among those patterns we can distinguish cases in which two domain walls, separating domains of dipoles with different polarization, are formed spontaneously and move irregularly in time. It turns out that the emergence of such patterns can be linked to the lowest energy saddle point of the interaction potential of the dipole chain. Moreover, for a large excitation energy, the dipole chain displays a strong sensitivity to the initial conditions, signifying its chaotic nature. We quantify the chaoticity of the system for different values of the excitation energy using a fast Lyapunov indicator.

The structure of the current paper is as follows. In Sec. II we present the Hamiltonian and the equations of motions of the dipole chain and discuss their equilibria. Linearizing these equations of motion around the GS, we arrive at the corresponding linear system whose properties are analyzed in Sec. III. The results for the energy transfer of a localized excitation are presented in Sec. IV and Sec. V. In particular, Sec. IV deals with the propagation of a low-energy excitation in the so-called weakly nonlinear regime, whereas Sec. V discusses the case of higher energy excitations in which the nonlinearity of the system is enhanced, leading to its chaotic behavior which is quantified by the Orthogonal Fast Lyapunov Indicator. Finally we provide our conclusions in Sec. VI.

II. THE HAMILTONIAN AND THE EQUILIBRIUM POINTS

We consider a linear chain of N identical rigid dipoles of electric dipole moment $\mathbf{d}_i = d \mathbf{u}_i$, which are fixed in space, separated by a constant distance a_i , and located along the X axis of the laboratory fixed frame (LFF) XYZ . The unit vectors $\mathbf{u}_i = (u_{X_i}, u_{Y_i}, u_{Z_i})$ determine the orientation of each dipole subjected to the holonomic constraint $|\mathbf{d}_i|^2 = d_{X_i}^2 + d_{Y_i}^2 + d_{Z_i}^2 = d^2$. The potential energy \mathcal{V}_{ij} between each pair (i, j) of rotors due to the mutual dipole-dipole interaction (DDI) is given by [32]

$$\mathcal{V}_{ij} = \frac{1}{4\pi\epsilon_0} \frac{(\mathbf{d}_i \cdot \mathbf{d}_j) r_{ij}^2 - 3(\mathbf{d}_i \cdot \mathbf{r}_{i,j})(\mathbf{d}_j \cdot \mathbf{r}_{i,j})}{r_{ij}^5} \quad (1)$$

with $\mathbf{r}_i = (X_i, Y_i = 0, Z_i = 0)$, $\mathbf{r}_{i,j} = \mathbf{r}_i - \mathbf{r}_j$ and $r_{ij} = |\mathbf{r}_{i,j}|$.

Here we assume periodic boundary conditions (PBCs) in the linear chain and we take into account only interactions between nearest neighbors (NNs), the total interaction potential \mathcal{V} of the system reads

$$\mathcal{V} = \sum_{i=1}^N \frac{1}{4\pi\epsilon_0 a_i^5} [(\mathbf{d}_i \cdot \mathbf{d}_{i+1}) a_i^2 - 3(\mathbf{d}_i \cdot \mathbf{r}_{i,i+1})(\mathbf{d}_{i+1} \cdot \mathbf{r}_{i,i+1})]. \quad (2)$$

It is convenient to express the total interaction potential \mathcal{V} in terms of the Euler angles ($0 \leq \theta_i \leq \pi$, $0 \leq \phi_i < 2\pi$) of each rotor, such that (2) takes the form

$$\mathcal{V}(\theta_i, \phi_i) = \alpha \sum_{i=1}^N [\cos \theta_i \cos \theta_{i+1} + \sin \theta_i \sin \theta_{i+1} \times (\sin \phi_i \sin \phi_{i+1} - 2 \cos \phi_i \cos \phi_{i+1})], \quad (3)$$

where $\alpha = d^2/4\pi\epsilon_0 a_i^3$ is the strength of the DDI. Note that the well-known stable *head-tail* configurations of the dipoles appear at $\theta_i = \pm\pi/2$ and $\phi_i = 0, \pi$. The rotational dynamics of the dipole chain is described by the Hamiltonian

$$H = \sum_{i=1}^N \frac{1}{2I} \left[p_{\theta_i}^2 + \frac{p_{\phi_i}^2}{\sin^2 \theta_i} \right] + \mathcal{V}(\theta_i, \phi_i), \quad (4)$$

where I is the moment of inertia of each dipole. The Hamiltonian (4) defines a dynamical system with $2N$ degrees of freedom $\{(\theta_i, p_{\theta_i}), (\phi_i, p_{\phi_i})\}_{i=1}^N$ where p_{θ_i}, p_{ϕ_i} denote the conjugate momenta of θ_i, ϕ_i , respectively. From the corresponding Hamiltonian equations of motion, it is easy to see that the manifolds \mathcal{N} and \mathcal{M} of codimension N given by

$$\mathcal{N} = \{(\theta_i, p_{\theta_i}) \mid \phi_i = \pi/2, 3\pi/2 \text{ and } p_{\phi_i} = 0\}, \quad (5)$$

$$\mathcal{M} = \{(\theta_i, p_{\theta_i}) \mid \phi_i = 0, \pi \text{ and } p_{\phi_i} = 0\} \quad (6)$$

are invariant under the dynamics, such that the number of degrees of freedom of the system is reduced to N . On the manifold \mathcal{N} , the rotational motion of each dipole is restricted to the corresponding YZ plane, and the Hamiltonian (4) becomes

$$H_{\mathcal{N}} = \sum_{i=1}^N \frac{p_{\theta_i}^2}{2I} + \alpha \sum_{i=1}^N \cos(\theta_i - \theta_{i+1}), \quad (7)$$

where the N polar angles θ_i vary in the interval $[-\pi, \pi)$. The Hamiltonian (7) describes the dynamics of an array of dipoles in the so-called altitudinal arrangement [37]. Moreover, the Hamiltonian (7) is equivalent to the 1D Hamiltonian describing the dynamics of XY spin chains [40–43], the latter constituting a canonical approach to the well-known XY Heisenberg Hamiltonian [44,45]. It is worth noticing that Hamiltonian (7) is structurally unstable in the sense that trajectories starting in the vicinity of the manifold \mathcal{N} tend to move away from it [38].

On the manifold \mathcal{M} , the Hamiltonian (4) reads

$$H_{\mathcal{M}} = \sum_{i=1}^N \frac{p_{\theta_i}^2}{2I} + \alpha \sum_{i=1}^N [\cos \theta_i \cos \theta_{i+1} - 2 \sin \theta_i \sin \theta_{i+1}], \quad (8)$$

and the motion of the dipoles takes place in the common polar XZ plane of constant azimuthal inclination $\phi_i = 0, \pi$ where the N angles θ_i vary in the interval $[-\pi, \pi)$. Following the same argumentation as for the Hamiltonian (7), the system described by (8) can be viewed as an alternative spin model. Contrary to the case of the manifold \mathcal{N} , the Hamiltonian (8) is structurally stable, since for weak enough perturbations away from the manifold \mathcal{M} and around the *head-tail* configuration, the dynamics takes place in the neighborhood of this configuration which is the absolute minimum of the potential $\mathcal{V}(\theta_i, \phi_i)$.

From now on, we focus on the planar dynamics arising from the Hamiltonian (8).

As mentioned above the stable *head-tail* configurations of the dipoles in the manifold \mathcal{M} appear for $\theta_i = \pm\pi/2$. For the sake of simplicity, we choose to move these equilibrium configurations to the origin $\theta_i = 0$ and to $\theta_i = \pi$, respectively. To this end, we introduce the following canonical transformation between the previous (θ_i, p_{θ_i}) and the new (x_i, p_i) coordinates

$$x_i = \theta_i - \pi/2, \quad p_i = p_{\theta_i}. \quad (9)$$

Employing this transformation, the Hamiltonian (8) obtains the form

$$H = \sum_{i=1}^N \frac{p_i^2}{2I} + \alpha \sum_{i=1}^N [\sin x_i \sin x_{i+1} - 2 \cos x_i \cos x_{i+1}], \quad (10)$$

where $p_i = I dx_i/dt$. Taking into account that our dipole chain model of Eq. (10) amounts essentially to the rigid rotor model used for the study of the dynamics of N interacting polar diatomic molecules [35–37], we find it convenient to express the energy, i.e., the Hamiltonian (10), in units of the molecular rotational constant $B = \hbar^2/2I$. To this end we define a new dimensionless time $t' = t/t_B$ with $t_B = \hbar/\sqrt{2}B$ whose use leads us to the following (dimensionless) Hamiltonian

$$E' = \frac{H}{B} = \sum_{i=1}^N \frac{p_i^2}{2} + \chi \sum_{i=1}^N [\sin x_i \sin x_{i+1} - 2 \cos x_i \cos x_{i+1}], \quad (11)$$

where $p_i' = dx_i/dt'$ and $\chi = \alpha/B$ is a dimensionless parameter controlling the dipole interaction. Besides the reduced energy $E' = H/B$, the dynamics of the system described by (11) depends also on the dipole parameter χ . However, this dependence can be removed by further rescaling the time, introducing $t'' = \sqrt{\chi} t'$. In terms of time t'' , the Hamiltonian (11) reads

$$E \equiv \mathcal{H} = \frac{H}{B\chi} = \sum_{i=1}^N \frac{p_i'^2}{2} + \sum_{i=1}^N [\sin x_i \sin x_{i+1} - 2 \cos x_i \cos x_{i+1}], \quad (12)$$

where $p_i'' = dx_i/dt''$, such that the dynamics only depends on the rescaled energy $E = H/B\chi$. The following study employs the Hamiltonian (12), and we omit the primes in order to simplify the notation.

We begin our exploration of the system's dynamics by addressing first its static properties regarding its equilibria, i.e., the roots of the N -dimensional gradient (critical points) of the potential

$$V = \sum_{i=1}^N [\sin x_i \sin x_{i+1} - 2 \cos x_i \cos x_{i+1}], \quad (13)$$

given by the system of equations ($\forall i = 1, 2, \dots, N$):

$$\frac{\partial V}{\partial x_i} = [\cos x_i \sin x_{i+1} + 2 \sin x_i \cos x_{i+1} + \cos x_i \sin x_{i-1} + 2 \sin x_i \cos x_{i-1}] = 0. \quad (14)$$

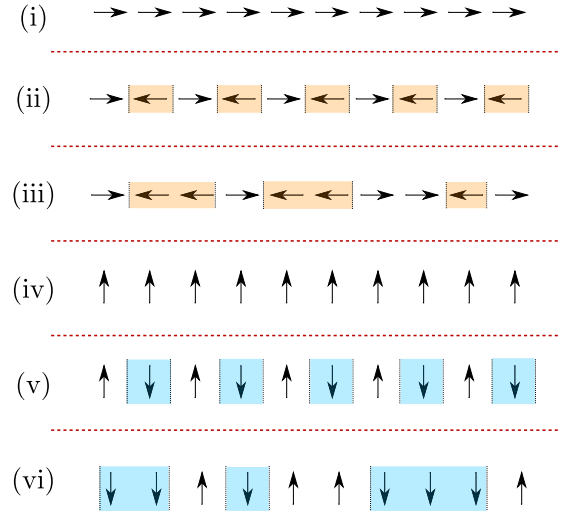


FIG. 1. Schematic representation of the six families of equilibrium points (i)–(vi) discussed in the main text in terms of the angle x_i .

A. Equilibrium points

From the inspection of Eqs. (14), we find the following critical points summarized in Fig. 1:

(i) The head-tail configuration of the dipoles $\{x_i = 0, \forall i\}$ or $\{x_i = \pi, \forall i\}$ [Fig. 1(i)]. This critical point is a minimum of the potential (13) (see the Appendix) with energy $E_m = -2N$. For the sake of simplicity, in the following we shift all the energies of the system by $2N$, such that this minimum energy becomes zero, i.e., $E_m = 0$.

(ii) The tail-tail and head-head configurations with alternating angles 0 and π , $\{x_i = \pi[1 \pm (-1)^i]/2, \forall i\}$ [Fig. 1(ii)]. These critical points are degenerate maxima of the potential (13) (see the Appendix) with energy $E_M = 4N$ (shifted by $2N$).

(iii) Configurations of alternating $2b$ blocks of an arbitrary number of dipoles n_i ($i = 1, 2, \dots, 2b$) where within each block i all n_i dipoles are either oriented as $x_k = \pi$ or $x_k = 0$. The potential energy of this configuration is E_m plus the potential energy excess of all pairs of dipoles left and right to the interfaces of two neighboring blocks with oppositely aligned dipoles. For our PBCs this adds up to the total energy $E_{s1} = 8b$ (shifted by $2N$). An example of such a configuration is shown in Fig. 1(iii) where, taking into account the PBCs, there are six blocks of dipoles with alternating polarization resulting in a total energy $E_{s1} = 24$.

These critical points are argued to be saddle points of rank $= 2b$ in the Appendix. In particular, for the maximum number of possible blocks, $2b = N$, we recover the configuration of maximum potential energy, $E_M = 4N$, which is indeed a critical point of rank $= N$. It is worth noting that all these saddle points are highly degenerate with respect to the length of the blocks and both their energy and their rank (number of negative eigenvalues of the Hessian), depend only on the number of blocks $2b$ and not on the number of dipoles n_i within each block.

(iv) The two configurations with $\{x_i = \pi/2, \forall i\}$ or $\{x_i = -\pi/2, \forall i\}$ [Fig. 1(iv)] which are saddle points (see the Appendix) with energy $E_{s2} = 3N$ (shifted by $2N$).

(v) The configurations with alternating $\pi/2$ and $-\pi/2$, $\{x_i = \pm(-1)^i \pi/2, \forall i\}$ [Fig. 1(v)] which represent saddle points (see the Appendix) with energy $E_{s3} = N$ (shifted by $2N$).

(vi) Configurations of alternating $2b$ blocks of an arbitrary number of dipoles n_i ($i = 1, 2, \dots, 2b$) where within each block i all n_i dipoles are either oriented as $x_k = \pi/2$ or $x_k = -\pi/2$. Following the same discussion as in the equilibrium configuration (iii), the potential energy of this configuration is $E_{s2} = 3N$ [case (iv)] minus the potential energy excess of all pairs of dipoles left and right to the interfaces of two neighboring blocks with opposite up and down aligned dipoles, such that the total energy is $E_{s4} = 3N - 4b$ (shifted by $2N$). An example of this configuration is shown in Fig. 1(vi) where, taking into account the PBC, there are six blocks of dipoles with alternating up and down orientation resulting in a total energy $E_{s4} = 18$.

The above six families of critical points (Fig. 1) allow one to get a glimpse of the high complexity of the landscape of the N -dimensional potential energy surface V [see Eq. 13]. The discussed energy hierarchy of these families should be reflected in the dynamics of the dipole chain. Indeed, and taking into account that for energy values below $E_{s1} = 8$ the phase space trajectories of the system remain trapped into the potential well around the minimum $E_m = 0$, we expect linear dynamics for small excitations around $E_m = 0$ and predominantly regular behavior for total excitation energies E below the energy of the lowest saddle point, i.e., for $E < \min(E_{s1}) = 8$. However, for $E > 8$, and due to the larger accessible phase space regions which involve also different equilibria, we expect to encounter a more complex nonlinear behavior. It is worth noting that for values of b close to one, the energy $E_{s1} = 8b$ of the corresponding saddle points is much smaller than the maximum energy $E_M = 4N$ of the potential V . Hence, one should expect a complex nonlinear behavior even for small excitation energies $E \gtrsim \min(E_{s1}) = 8$.

In the following, we present results for the dynamics of the dipole chain for different excitation energies, spanning the three aforementioned regions with qualitatively different dynamical behavior, i.e., the linear ($E \ll 8$), the regular ($E \lesssim 8$), and the irregular ($E \gtrsim 8$) regime.

III. THE LINEAR BEHAVIOR

The equations of motion of the Hamiltonian (12) can be written as

$$\ddot{x}_i = -(\cos x_i \sin x_{i+1} + 2 \sin x_i \cos x_{i+1} + \cos x_i \sin x_{i-1} + 2 \sin x_i \cos x_{i-1}). \quad (15)$$

For low-energy excitations, e.g., small oscillations around the head-tail equilibrium configuration $\{x_i = 0, \forall i\}$ or $\{x_i = \pi, \forall i\}$ of minimum energy E_m , the linear approximation of the equations of motion (15) yields

$$\ddot{x}_n = -(x_{n-1} + 4x_n + x_{n+1}), \quad n = 1, \dots, N. \quad (16)$$

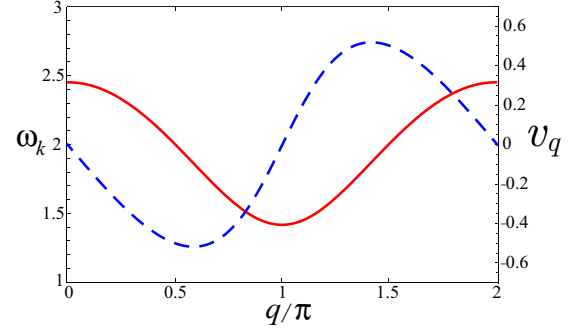


FIG. 2. Dispersion relation ω_k (red solid curve) and group velocity v_q (blue dashed curve) as a function of q/π with $q = 2\pi k/N$ being the wave number.

As it is well known, the system of linear differential equations (16) can be solved in terms of N normal modes (Q_k, P_k) [46],

$$Q_k(t) = \frac{1}{\sqrt{N}} \sum_{n=1}^N x_n(t) \exp\left(i \frac{2\pi kn}{N}\right), \quad k = 1, \dots, N,$$

$$P_k(t) = \frac{1}{\sqrt{N}} \sum_{n=1}^N p_n(t) \exp\left(i \frac{2\pi kn}{N}\right), \quad k = 1, \dots, N, \quad (17)$$

where $p_n(t) = \dot{x}_n(t)$.

In the normal mode variables (Q_k, P_k), the Hamiltonian H_0 associated to the linear system (16) reads

$$H_0 = \sum_{k=1}^N \mathcal{E}_k = E_0, \quad \mathcal{E}_k = \frac{1}{2}(|P_k|^2 + \omega_k^2 |Q_k|^2),$$

$$k = 1, \dots, N, \quad (18)$$

where ω_k and \mathcal{E}_k are the frequency and the (harmonic) energy of each normal mode, respectively. The sum of the energies of all normal modes $\{\mathcal{E}_k\}$ yields the total harmonic energy E_0 , corresponding to the Hamiltonian H_0 of the linearized system (16). The frequency ω_k relates to the wave number k through the dispersion relation

$$\omega_k = \sqrt{4 + 2 \cos q}, \quad q = \frac{2\pi k}{N} \quad (19)$$

derived from Eqs. (16) and (17). The above expression [Eq. (19)] has already been deduced in e.g., the study of molecular chains [35] and has the form depicted in Fig. 2 (red solid line). As expected, the frequency ω_k is 2π -periodic with q , and it enjoys a reflection symmetry with respect to $q = 0$ and π . As we can observe in Fig. 2 (red solid line), the linear spectrum is optic-like with the frequency ω_k possessing an upper bound (maximum) $\omega_k = \sqrt{6}$ for $q \rightarrow 0$ (long-wavelength limit) and a lower bound (minimum) $\omega_k = \sqrt{2}$ for $q = \pi$ (short-wavelength limit).

From the dispersion relation (19), the group velocity v_q of the normal modes can be derived

$$v_q = \frac{d\omega_k}{dq} = -\frac{\sin q}{\omega_k}. \quad (20)$$

As shown in Fig. 2 (blue dashed line), v_q vanishes when ω_k reaches its maximum or minimum value, indicating that the normal modes with the longest and the shortest wavelengths are nonpropagating modes. In contrast, for $q/\pi = \arccos(-2 + \sqrt{3})/\pi \approx 0.59$ and $q/\pi = 1 + \arccos(2 - \sqrt{3})/\pi \approx 1.41$ the group velocity reaches its maximum amplitude $|v_q| \approx 0.52$, rendering the corresponding normal modes the fastest propagating ones in the system.

In the current study we are interested in the time propagation of single dipole excitations through the dipole chain for different values of the excitation energy. More specifically, starting from the head-tail configuration [Fig. 1 (i)] of minimal energy $E_m = 0$, we excite at $t = 0$ a single dipole, supplying it with an excess energy ΔK . In all our calculations we use a chain of 200 dipoles with PBC, a fact that allows us to excite a specific dipole (here the 100th) without loss of generality. The initial conditions $(x_i(0), p_i(0))$ of our system at $t = 0$ are given therefore by

$$x_i(0) = p_i(0) = 0, \quad \text{for } i \neq 100,$$

$$\Delta K = \frac{p_{100}(0)^2}{2} + 4[1 - \cos x_{100}(0)]. \quad (21)$$

Using these initial conditions, we investigate the time propagation of the excitation by integrating numerically the equations of motion (15) for the dipole chain. In order to achieve a high accuracy, we integrate Eqs. (15) using an explicit Dormant-Prince Runge-Kutta algorithm of eighth order with step size control and dense output [47]. The results of these integrations are subsequently compared to those extracted by a symplectic and symmetric Gauss method of six stages [48]. Up to the same prescribed error tolerances, in all cases the numerical results obtained with both methods are the same.

During the integration we record at each time step, besides the phase space variables $x_i(t)$ and $p_i(t)$ of each dipole, also the harmonic energy contribution $\mathcal{E}_k(t) = \frac{1}{2} [|P_k(t)|^2 + \omega_k^2 |Q_k(t)|^2]$ of each Fourier mode $(Q_k(t), P_k(t))$ resulting from the Fourier transform [Eq. (17)] of the numerically extracted $\{x_i(t), p_i(t)\}$. We emphasize here that all these quantities are recorded for the exact equations of motion [Eq. (15)] of our system and not for their linearized form [Eq. (16)] discussed above.

As we have briefly mentioned in the previous section, for very low values of the excitation energy $\Delta K \ll 8$ (much lower than the energy of the first saddle point) we expect a linear behavior of the dipole chain, with Eq. (16) describing appropriately the small oscillations of the dipoles around the head-tail equilibrium configuration. In this linear regime, the harmonic energy $\mathcal{E}_k(t)$ stored in each Fourier mode $(Q_k(t), P_k(t))$ remains almost constant in time, since the Fourier modes are the approximate (uncoupled) normal modes of the system, and therefore the total excitation energy ΔK is roughly equal to the total harmonic energy $E_0(t) = \sum_{k=1}^N \mathcal{E}_k(t)$ distributed among the N Fourier modes of the system [see Eq. (18)].

For larger excitation energies ΔK the behavior of the system is expected to be in general nonlinear, involving a transfer of energy between the different Fourier modes $(Q_k(t), P_k(t))$ due to their coupling. The higher the degree of such a nonlinear mode-coupling, the higher we expect to be the deviation

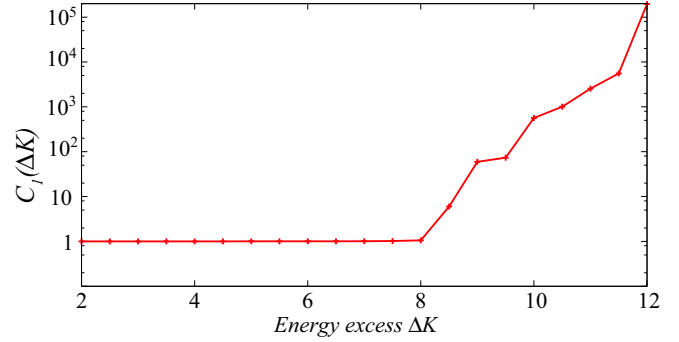


FIG. 3. Dependence of $C_1(\Delta K)$ [see Eq. (22)] on the excitation energy ΔK for a single initially excited dipole [Eq. (21)]. Each point of the curve corresponds to the average over an ensemble of 40 simulations with the same initial excess energy but for different initial conditions. Note that a logarithmic scale scale is used for $C_1(\Delta K)$.

of ΔK (the total energy of our system, involving all the couplings between the modes) from the total harmonic energy contribution $E_0(t)$ resulting from the modes $(Q_k(t), P_k(t))$ which are assumed to be uncoupled. Therefore, we can use this deviation between ΔK and $E_0(t)$ as an indicator of the degree of nonlinearity in the system.

In particular, we define the function $C_1(\Delta K)$

$$C_1(\Delta K) = \frac{\langle E_0 \rangle}{\Delta K}, \quad \langle E_0 \rangle = \frac{1}{t_f} \int_0^{t_f} E_0(t) dt, \quad (22)$$

where $\langle E_0 \rangle$ is the time average of the total harmonic energy $E_0(t)$ of the Fourier modes $\{Q_k(t), P_k(t)\}$ up to a (large) final time t_f . According to our above discussion $C_1(\Delta K) = 1$ for a linear system, where the Fourier modes, coinciding with its normal modes, are uncoupled. The closer the function $C_1(\Delta K)$ is to 1, the closer the exact dynamics of the system is expected to be to linear.

We present in Fig. 3 the behavior of $C_1(\Delta K)$ for excess energies $\Delta K \in [2, 12]$. Apart from the time average in the definition of $C_1(\Delta K)$ [Eq. (22)], we have also performed for each point of Fig. 3 an average over 40 different sets of initial conditions [different choices of $x_{100}(0)$ and $p_{100}(0)$, all corresponding to the same excess energy ΔK ; see Eqs. (21)]. The value of the final time t_f considered here reads $t_f = 5000$, which is sufficiently large compared to the intrinsic timescales of the system. Indeed, since the lowest frequency of the linear spectrum and the maximal group velocity are respectively $\omega_k \approx 1.5$ and $v_q \approx 5$ (see Fig. 2) the final time $t_f = 5000$ roughly corresponds to 1200 harmonic oscillation periods, and it is almost 25 times longer than the typical time a localized excitation in the system needs to travel from the central to the outer part of the chain.

We observe (Fig. 3) that for $\Delta K < 8$ the dynamics of the system is only weakly nonlinear, since the average of the total harmonic energy contribution $\langle E_0 \rangle$ of the Fourier modes is a good approximation to the total energy ΔK of the system [$C_1(\Delta K) \approx 1$]. In this region we expect that the linear normal modes couple only weakly, leading to minor energy transfer between different modes, but keeping the corresponding harmonic total energy $E_0(t)$ approximately constant, equal to ΔK .

In contrast, for excess energies $\Delta K > 8$ the value of $C_1(\Delta K)$ increases rapidly, with the average total harmonic

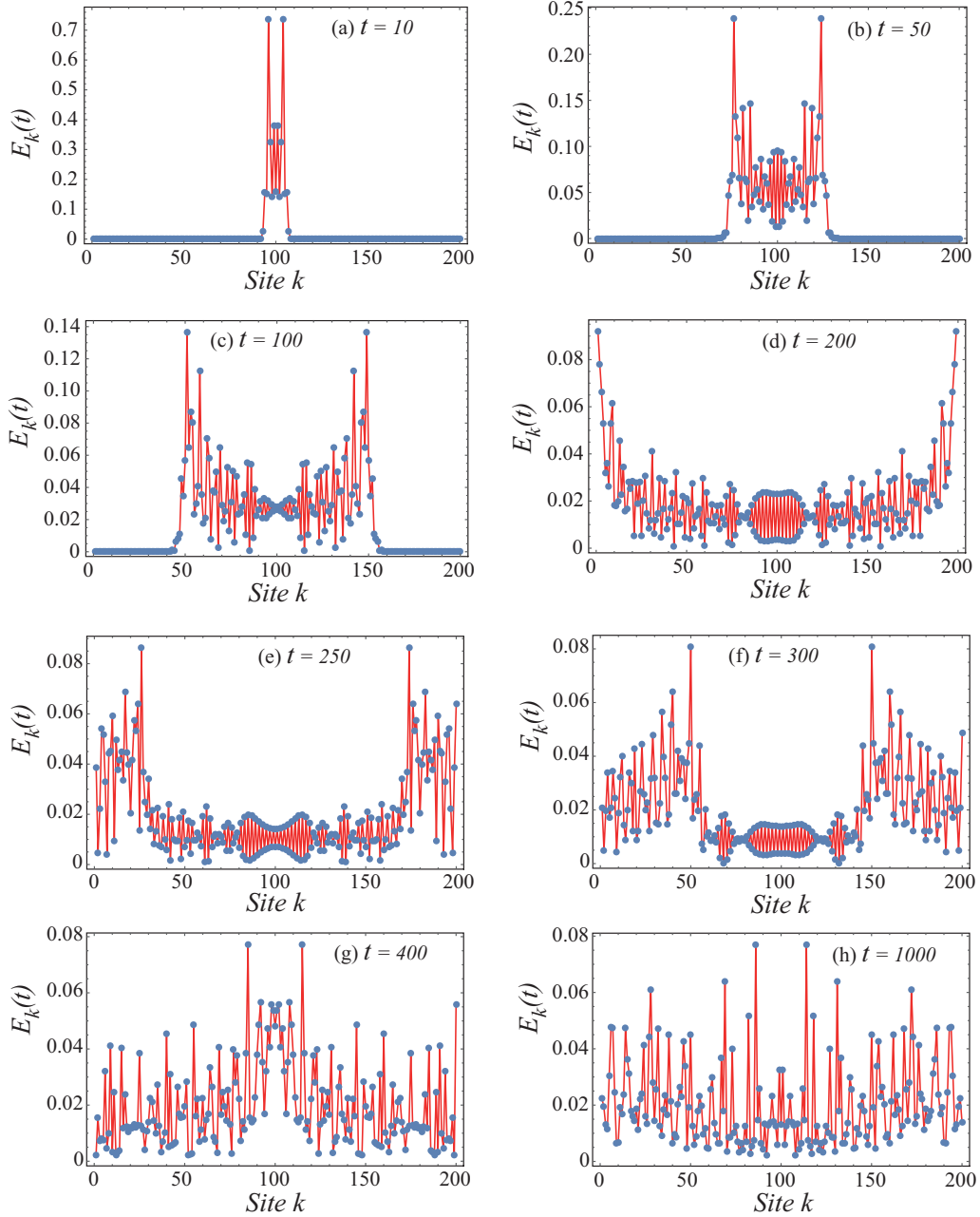


FIG. 4. Spatial (site) distribution of the local energies $E_k(t)$ for different time instants. The number of dipoles in the chain is $N = 200$ and the initial kinetic energy excess provided to the central dipole at site 100 is $\Delta K = 4$.

energy $\langle E_0 \rangle$ of the Fourier modes obtaining much larger values than the total excitation energy ΔK , a fact that indicates a highly nonlinear behavior. Although the value $\Delta K = 8$ cannot be considered as a precise threshold between the regimes of a weakly and a highly nonlinear behavior, this value can be perceived as an upper bound, above which the system reacts to localized energy excitations in a highly nonlinear way. It is worth noting that this upper bound ($\Delta K \approx 8$) coincides with the energy $E_{s_1} = 8$ of the lowest saddle point consisting of two blocks of dipoles with opposite polarization. After overcoming the energetic barrier of the first saddle point, the available phase space of the system increases dramatically, offering possibilities for various dynamical behaviors. Interestingly, we see that the total harmonic energy contribution E_0 of the

Fourier modes is always larger than the total energy $E \equiv \Delta K$ of the system. In other words, the contribution of the coupling between the Fourier modes to the energy, representing the nonlinear interaction, is negative, e.g., it is attractive. Interestingly, the fourth-order expansion of the total potential V [Eq. (13)] around the equilibrium position $\{x_i = 0, \forall i\}$ yields

$$V \approx \sum_{i=1}^N (x_i^2 + x_{i+1}^2 + x_i x_{i+1}) - \sum_{i=1}^N \left[\frac{(x_i^2 + x_{i+1}^2)(x_i + x_{i+1})^2}{12} + \frac{x_i^2 x_{i+1}^2}{3} \right], \quad (23)$$

where the negative energy contribution of the nonlinear terms to the total potential energy is clearly observed.

IV. THE WEAKLY NONLINEAR REGIME

In this section we present in detail the response of the dipole chain to single local perturbations in the weakly nonlinear regime of small excitation energies ($\Delta K < 8$). Following a similar scheme as in Sec. III, given a chain of 200 dipoles with PBC in the head-tail configuration of minimal energy $E_m = 0$, we locally excite at $t = 0$ the 100th dipole of the chain by supplying it with an excess of kinetic energy ΔK . Thus, the initial conditions $(x_i(0), p_i(0))$ of our system at $t = 0$ read

$$\begin{aligned} x_i(0) &= p_i(0) = 0, & \text{for } i \neq 100, \\ x_{100}(0) &= 0, & p_{100}(0) = \sqrt{2\Delta K}. \end{aligned} \quad (24)$$

In order to study the propagation of this initially localized excitation along the dipole chain we calculate numerically the time evolution of the local energies $E_k(t)$:

$$\begin{aligned} E_k(t) &= \frac{p_k(t)^2}{2} + \frac{1}{2}[\sin x_k(t) \sin x_{k+1}(t) - 2 \cos x_k(t) \cos x_{k+1}(t) \\ &+ \sin x_k(t) \sin x_{k-1}(t) - 2 \cos x_k(t) \cos x_{k-1}(t)], \end{aligned} \quad (25)$$

which indicate the amount of energy stored in each dipole in relation to its NNs.

The local energy profiles for $\Delta K = 4$ at different time instants shown in Fig. 4 provide a glimpse of the different steps of the excitation propagation. Shortly after the excitation, most of the excess energy is transferred to the NNs of the initially excited dipole (100th), which become the main energy carriers initiating the energy spreading along the chain. Indeed, at short times $t = 10, 50$ and 100 [see Figs. 4(a)–4(c)], the excitation transfer is clearly induced by two (symmetric) energy fronts that propagate along the chain. At $t \approx 200$, the energy excitation reaches the ends of the chain [see Fig. 4(d)] having transferred an amount of energy to every dipole in the chain, causing their oscillations. This yields a propagation velocity $v_p \approx 0.5$, close to the maximum value of the group velocity $|v_q| \approx 0.52$ found for the linear case [see Eq. (20)].

Due to the PBC of the system for $t \gtrsim 200$ the excitation continues its propagation from the outer dipoles (at sites 1, 200) to the inner ones (located at sites around 100), i.e., the direction of propagation is reversed such that for $t \approx 400$ the excitation reaches again the central dipoles of the chain [see Figs. 4(e)–4(g) corresponding to $t = 250, 300$, and 400]. As the chain is progressively excited, the sharp intensity peaks of the propagation fronts observed at short times [Fig. 4(a)] decays significantly [Fig. 4(e)], indicating that the system tends to thermalize, reaching for long times energy equipartition [see Fig. 4(h) for $t = 1000$].

According to the above discussion, a global picture of the time evolution of the local energy $E_k(t)$ is given in terms of a color map in Fig. 5(a). After the 100th dipole is excited with an excess energy $\Delta K = 4$, the excitation energy is gradually distributed along the chain by means of the two aforementioned symmetric energy fronts. As the system approaches the energy

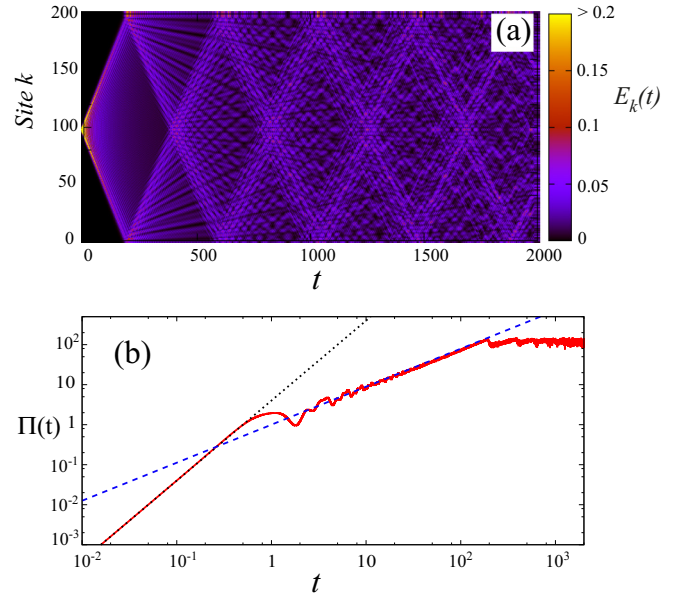


FIG. 5. (a) Time evolution of the local energy $E_k(t)$ of the dipoles (depicted by color). The number of dipoles in the chain is $N = 200$ and the initial kinetic energy excess provided to the central dipole at site 100 is $\Delta K = 4$. (b) Time evolution of the participation ratio $\Pi(t)$ [Eq. (26)], depicted by the solid red line, for $N = 200$ and $\Delta K = 4$. The black dotted and the blue dashed lines indicate the very short initial superballistic energy spreading $\Pi(t) \propto t^2$ and the intermediate nearly ballistic energy propagation $\Pi(t) \propto t^\alpha$ with $\alpha = 0.95$, respectively. Note that a double logarithmic scale is used.

equipartition state, the energy fronts are distorted and their intensity decreases.

To quantify the localization of the energy along the chain, we use the participation ratio [49]

$$\Pi(t) = \frac{\Delta K^2}{\sum_{k=1}^N E_k(t)^2} - 1, \quad (26)$$

with E_k being the local energies given by Eq. (25). When the excitation is maximally localized, i.e., the total excitation energy ΔK of the system is carried by a single dipole, the value of $\Pi(t)$ is zero, while if there is complete equipartition ($E_k \approx \Delta K/N \forall k$) $\Pi(t) = N - 1$. The time evolution of $\Pi(t)$ is shown in Fig. 5(b). Starting from a fully localized excitation ($\Pi(0) = 0$), we observe in Fig. 5(b) a short transient ($t \lesssim 0.5$) where the participation ratio grows as $\Pi(t) \propto t^2$. This quadratic increase of $\Pi(t)$ indicates a superballistic spreading of the excitation in the first period of the time evolution, a transport behavior encountered also in other setups, e.g., in the case of quantum excitations coupled to spatially extended many-body systems [49]. In the time interval $0.5 \lesssim t \lesssim 5$, the superballistic behavior is gradually lost such that, in the interval $5 \lesssim t \lesssim 200$, the energy transfer exhibits a nearly ballistic trend which is characterized by an almost linear behavior, i.e., $\Pi(t) \propto t^\alpha$ with $\alpha = 0.95$. For $t \gtrsim 200$, after the excitation has reached the boundaries of the dipole chain, Fig. 5(b) shows a plateau $\Pi(t) \approx 125$, indicating that the system has reached a regime where the excitation energy is almost equally partitioned among all the dipoles.

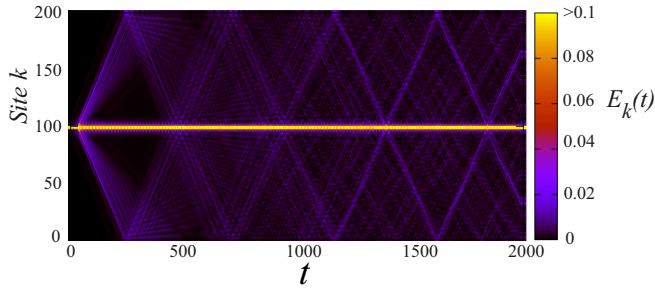


FIG. 6. Time evolution of the local energy $E_k(t)$ of the dipoles (depicted by color). The number of dipoles in the chain is $N = 200$, and the initial kinetic energy excess given to the central dipole 100 is $\Delta K = 12$.

V. THE HIGHLY NONLINEAR REGIME

Following the same scheme as in Sec. IV, we excite at $t = 0$ the 100th dipole from the head-tail ground state of a 200-dipole chain, supplying it with a kinetic energy excess $\Delta K > 8$.

A typical propagation scheme in this highly nonlinear regime is the one obtained for an excess energy $\Delta K = 12$. For this value the time evolution of the spatial distribution

of the local energies $E_k(t)$, $k = 1, 2, \dots, 200$ is depicted in Fig. 6. We observe a robust excitation around the 100th dipole, indicating that the system does not reach energy equipartition up to long times. Indeed, the initially excited dipole 100 shares predominantly energy with a few of its neighbors so that a significant part of the excess energy remains localized around it.

This fact is emphasized in Fig. 7 where the local energy profiles for $t = 40, 50, 100, 500, 1000$, and 2000 are depicted. At short times [see Fig. 7(a) for $t = 40$], the excitation is mostly trapped in the initially excited central dipole. For $t = 50$, an emerging propagation front is observed in Fig. 7(b), whose energy, after some time [see Fig. 7(c)] is gradually distributed among all the other dipoles of the chain. However, no further significant energy spreading is observed for $t \geq 500$ in Figs. 7(d)–7(f), such that the excitation energy of the few central dipoles (close to the initially excited one) remains always much larger than that of the other dipoles, creating overall a highly localized profile which persists in time [see Figs. 7(e) and 7(f)].

As in the previous section, the time evolution of the participation ratio $\Pi(t)$ [Eq. (26)], depicted in Fig. 8(a), provides a more detailed description of how the initial excess

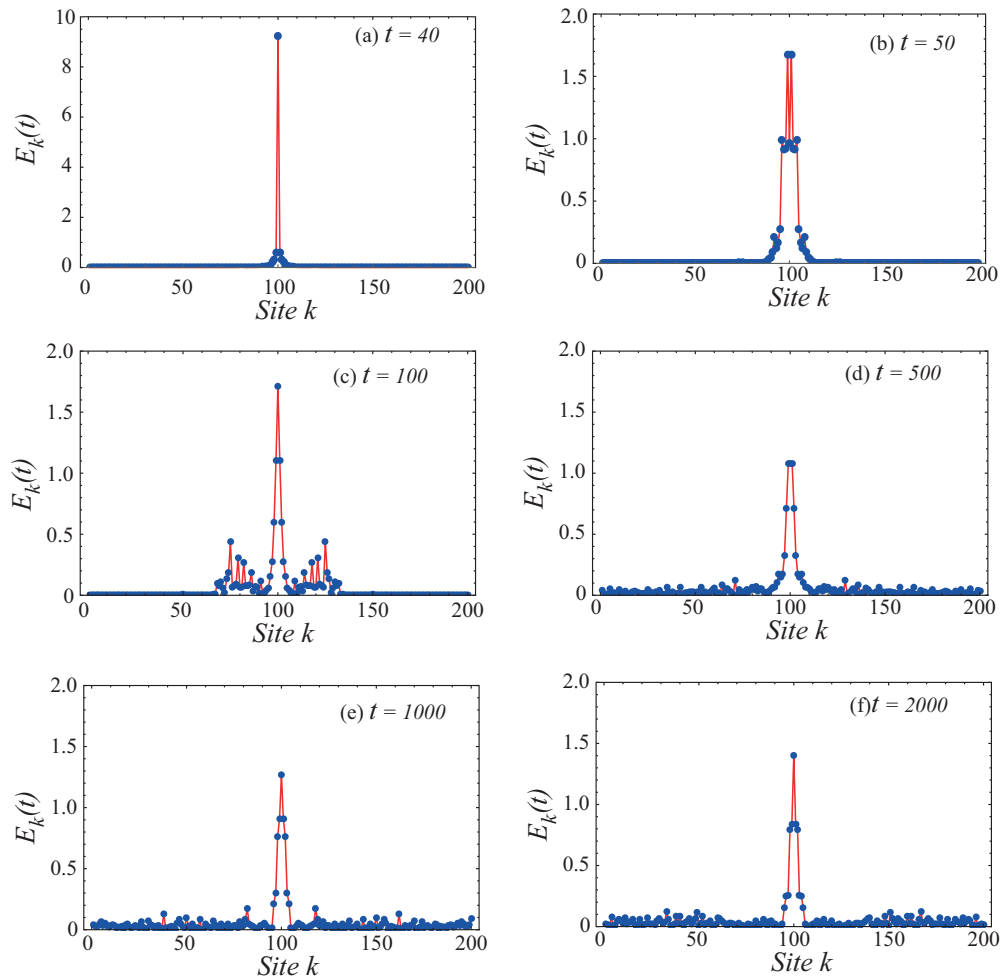


FIG. 7. Spatial (site) distribution of the local energies $E_k(t)$ for different time instants. The number of dipoles in the chain is $N = 200$, and the initial kinetic energy excess given to the central dipole at site 100 is $\Delta K = 12$.

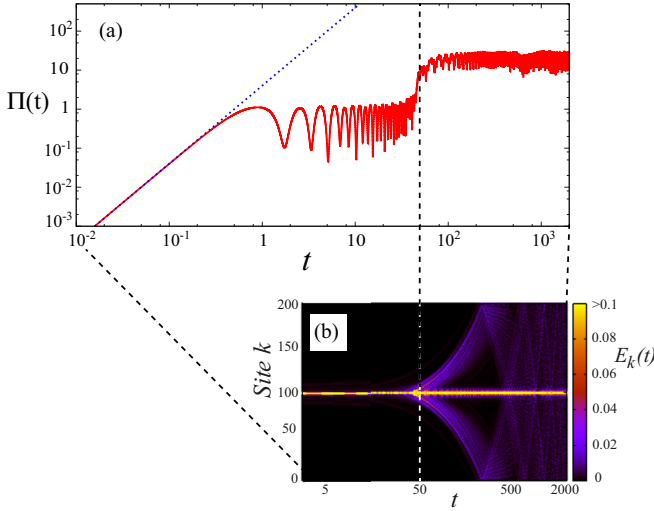


FIG. 8. (a) Time evolution of the participation ratio $\Pi(t)$ [Eq. (26)], depicted by the solid red line, for $N = 200$ and $\Delta K = 12$. The blue dotted line indicates the very short initial superballistic energy spreading $\Pi(t) \propto t^2$. Note that the results are presented in a log-log plot. (b) Time evolution of the local energy $E_k(t)$ of the dipoles, depicted by color. Note that a logarithmic scale is used in the horizontal axis of the color map, accounting for the time t .

energy $\Delta K = 12$ propagates along the chain. Similarly to the case of smaller excitation energies [Fig. 5(b)], the energy spreading presents a very short superballistic transient ($t \lesssim 0.5$) characterized by a quadratic increase $\Pi(t) \propto t^2$. After this transient, during the interval $0.5 \lesssim t \lesssim 50$ the participation ratio enters an oscillatory state around $\Pi(t) \approx 0.5$. This state corresponds to the intense localized mode around the central dipole observed in Fig. 6 and in Fig. 7(a) where almost only the central dipole 100 is excited. As we observe in Fig. 8(a), this steady state abruptly breaks at $t \approx 50$, causing the participation function to jump to a higher oscillatory steady state around $\Pi(t) \approx 10$. This new steady state is the outcome of the energy spreading events discussed along with Figs. 7(c)–7(f). Up to some extent, the abrupt jump of $\Pi(t)$ at $t \approx 50$ can be inferred from the difference between the profiles of the spatial distribution of the local energies $E_k(t)$ for $t = 40$ and $t = 50$ [Figs. 7(a) and 7(b)]. More specifically, such a jump indicates that at a certain time around $t \approx 50$, a small amount of energy starts to diffuse along the chain. This trend can be clearly observed when the color map of Fig. 6, depicting the time evolution of the spatial distribution of the local energies $E_k(t)$, is presented in a logarithmic time scale [Fig. 8(b)]. Such a representation shows [Fig. 8(b)] that up to $t \lesssim 50$ most of the excitation is trapped in the central dipole, whereas for $t \gtrsim 50$ a small amount of energy starts spreading along the dipole chain, with its major part remaining, nevertheless, localized in the vicinity of the central dipole.

This high degree of the energy localization observed in Figs. 6 and 7 suggests the existence of a strong nonlinearity since, for the linear case the dispersion of the excitation energy along the complete chain dominates the dynamics, leading to an approximately equipartition regime in terms of local energies E_k . Even more, it turns out that the localization of the excitation energy in Figs. 6 and 7 can be linked

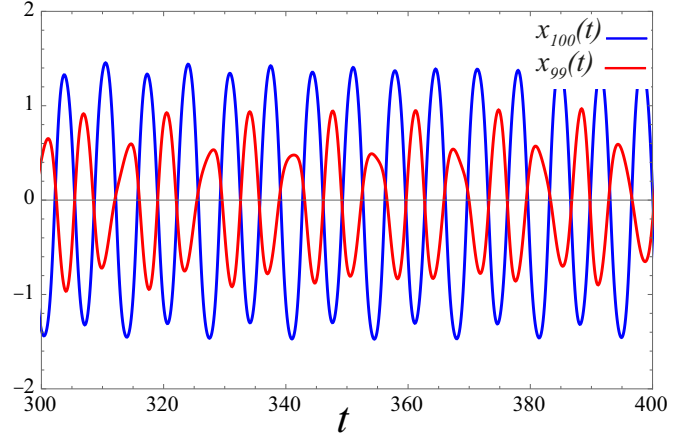


FIG. 9. Time evolution of the angles $x_{99}(t)$ and $x_{100}(t)$ of the dipoles 99 and 100 in the interval $300 \leq t \leq 400$. Excess energy is $\Delta K = 12$.

to discrete breather solutions of the nonlinear equations of motion of our system [Eq. (15)]. Briefly speaking, a discrete breather is a spatially localized *exact* periodic solution of the nonlinear equations of motion of a given discrete lattice (for more details, we refer the reader to Refs. [14,15]). The nonresonant condition between the frequency Ω of a breather solution and the dispersion relation ω_k prevents the existence of breathers with a frequency in the linear spectrum, such that the breather frequency Ω should always lie outside the linear spectrum ω_k . Such breather solutions have been shown to exist, among others, in many models featuring magnetic interactions similar to the ones considered here, including ferromagnetic Heisenberg spin chains [44,45] and systems of coupled magnetic pendulums [50].

In our system, for $\Delta K = 12$, we have seen (Fig. 7) that a major part of the excitation energy ΔK stored initially on the 100th dipole remains localized in the few dipoles surrounding it up to long times. Moreover, when the time evolution of the angles $x_{99}(t)$ and $x_{100}(t)$ of the dipoles 99 and 100 respectively are examined (see Fig. 9), we find that their motion is in both cases fairly periodic (oscillatory) with a period of $\tau \approx 6.7$. The periodicity of these oscillations is justified by Fig. 10, where the Fourier spectra of $x_{99}(t)$ and $x_{100}(t)$ are depicted. Indeed, we observe that these spectra exhibit a strong peak at a frequency $f \approx 0.15$ (with its symmetric counterpart at $f \approx 0.85$), reflecting the fact that the corresponding signals can be approximated as oscillations with a single frequency $\Omega = 2\pi f \approx 2\pi \times 0.15 \approx 0.94$, corresponding to a period of $\tau \approx 6.67$. Since this oscillation frequency, $\Omega \approx 0.94$, is outside (more precisely below) the linear spectrum depicted in Fig. 2 (red line), we have strong evidence that the localized excitation of the dipole chain observed in Figs. 6 and 7 during its time evolution corresponds to a discrete breather.

Besides the typical discrete breather pattern of energy localization shown in Fig. 6, the dipole chain exhibits additional propagation schemes, depending on the value of the initial excitation energy ΔK , all of them involving a high degree of energy localization. The time evolutions for the local energies $E_k(t)$ for four cases $\Delta K = 10.776, 11.128, 10.2$, and 11.12 , corresponding to different propagation patterns, are shown in

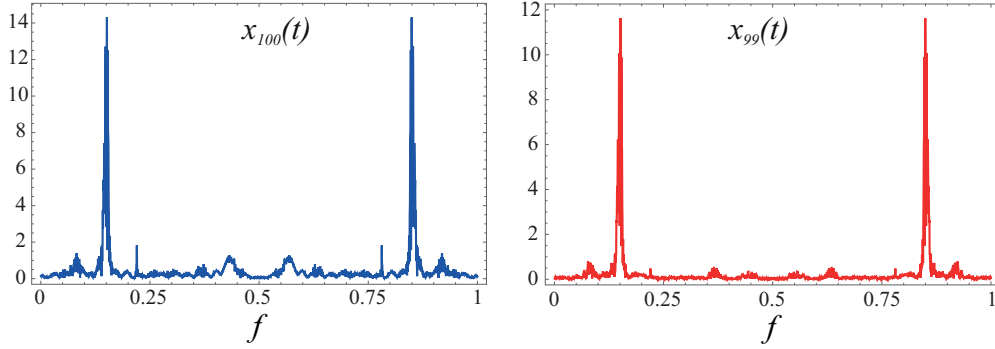


FIG. 10. Fourier spectra of $x_{99}(t)$ and $x_{100}(t)$ of the dipoles 99 and 100. The excess energy $\Delta K = 12$ is provided to the 100th dipole.

Figs. 11(a)–11(d). The main difference between these is the behavior of the principal energy carriers, i.e., the dynamics of those sites that carry the largest amount of excitation energy. For $\Delta K = 10.776$ and 11.128 [Figs. 11(a) and 11(b)], the energy of the system is highly localized in two energy carriers that follow trajectories of a regular periodic character. In contrast, for $\Delta K = 10.2$ and 11.12 [Figs. 11(c) and 11(d)] the principal energy carriers follow rather complex trajectories which, given their strong localization and complexity, could be linked to the so-called chaotic breathers [16]. Contrary to the concept of a discrete breather as a localized excitation which is a solution of the nonlinear equations of motion of the lattice, a chaotic breather is an excitation of chaotic nature that may appear as a response to initial local excitations of the lattice, a situation that, as it will be argued below, bears strong similarities to the one described here regarding the propagation of a localized excitation in our dipole chain in the highly nonlinear regime ($\Delta K \gtrsim 8$).

Apart from the different patterns of energy propagation observed in Fig. 11 for the different values of ΔK , it turns

out that also the configurations $\{x_k\}$ evolve differently in time. We illustrate this fact in Fig. 12 where the time evolution of $\cos[x_k(t)]$ is shown for the same excitation energies, $\Delta K = 10.776, 11.128, 10.2,$ and 11.12 , as those considered in Fig. 11. For $\Delta K = 10.776$ and 11.128 [see Figs. 12(a) and 12(b)] we observe the expected behavior: except for the energy-carrying rotors (ECRs), which exhibit fast long-amplitude oscillations (fast changing x_k) while propagating along the chain leading to the corresponding traces in Figs. 12(a) and 12(b), all the remaining dipoles are mainly polarized in the same direction [$x_k = 0$] [$\cos(x_k) = 1$] as in the ground state configuration.

In contrast, for $\Delta K = 10.2$ and 11.12 [Figs. 12(c) and 12(d)] the situation is dramatically different. Instead of a single polarized region ($\cos(x_k) = 1$), like the yellow background in Figs. 12(a) and 12(b), two regions of opposite polarization [$\cos(x_k) = 1$ and $\cos(x_l) = -1$] emerge during the time evolution. These regimes of locked phases ($\{x_k = 0\}$ and $\{x_l = \pi\}$, respectively) corresponding to domains of opposite polarization appear spontaneously and they are dynamically separated by two propagating domain walls provided by the

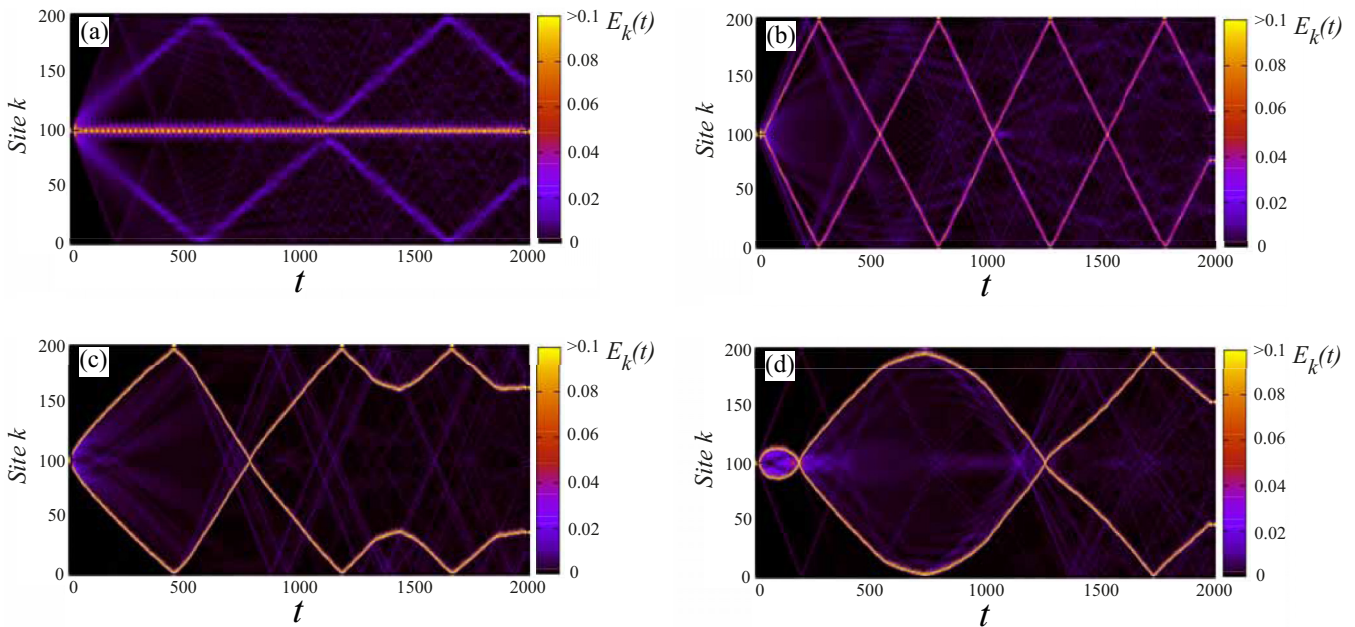


FIG. 11. Time evolution of the local energy $E_k(t)$ of the dipoles (depicted by color) for four values of the excess energy: (a) $\Delta K = 10.776$, (b) $\Delta K = 11.128$, (c) $\Delta K = 10.2$, and (d) $\Delta K = 11.12$.

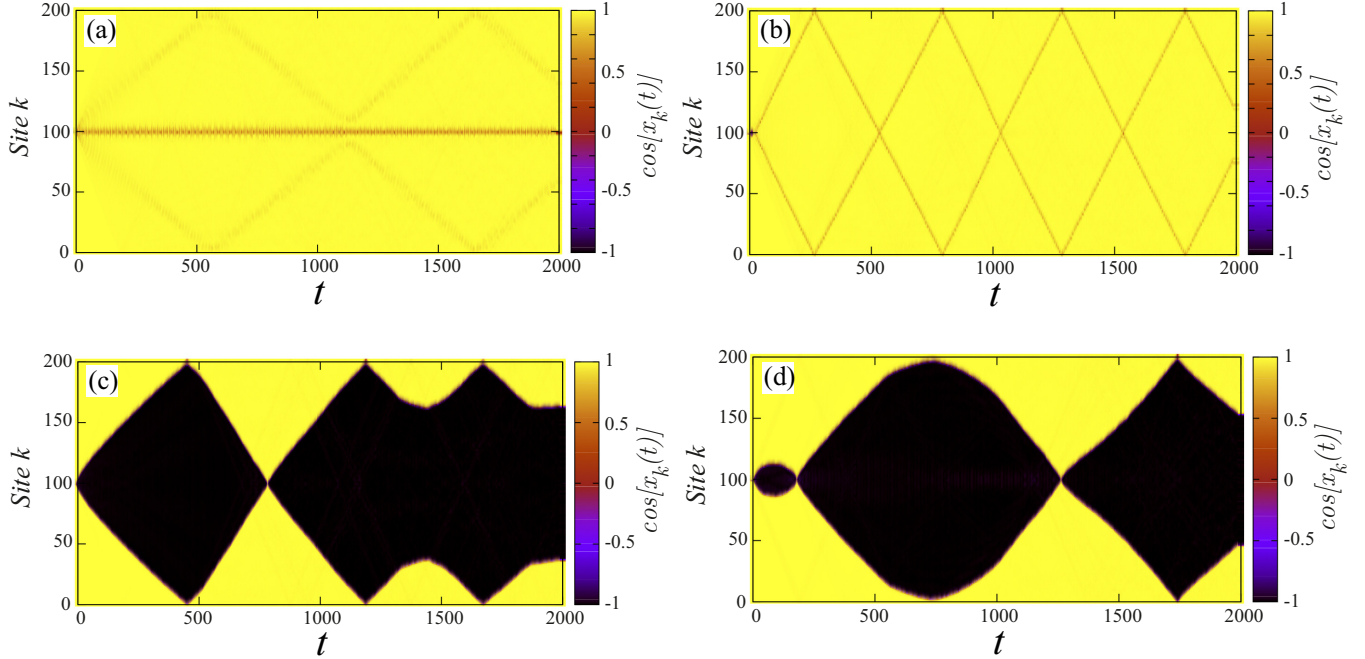


FIG. 12. The time evolution of $\cos(x_k)$ (depicted by color) for different values of the excess energy ΔK : (a) $\Delta K = 10.776$, (b) $\Delta K = 11.128$, (c) $\Delta K = 10.2$, and (d) $\Delta K = 11.12$ as in Fig. 11.

two fast rotating ECRs [compare Figs. 12(c) and 12(d) with Figs. 11(c) and 11(d)]. In particular, in the course of the dynamics, the dipoles lying between the two ECRs spontaneously flip, forming a domain of opposite polarization [$\cos(x_i) = -1$, black region in Figs. 12(c) and 12(d)] compared to that of the ground state [yellow region in Figs. 12(c) and 12(d)].

Although the origin of this spontaneous phase locking is not entirely clear, it can be related to the existence of the lower saddle point equilibria of energy $E_{s_1} = 8 < \Delta K$ [$b = 1$, Sec. II A (iii)]. This assumption relies on the resemblance of the topology between the phase locked states and the highly degenerate saddle point equilibrium configurations consisting of two blocks: one with a given number n of dipoles with $x_i = \pi$ and another with the remaining $N - n$ dipoles polarized along $x_k = 0$. As mentioned in Sec. II, all such saddle points, consisting of two domains of opposite polarization are highly degenerate, since their total potential energy $E_{s_1} = 8$ depends only on the number of domain walls (here two) and not on the number of dipoles on each domain (n and $N - n$, respectively). With an excitation energy $\Delta K = 12 > E_{s_1}$ a spontaneous dynamical transition from the fully polarized ground state to the first saddle point is energetically possible and therefore can occur for certain initial conditions [Figs. 12(c) and 12(d)]. During the time evolution of such a state the domain walls, identified with the ECRs, shift [Figs. 12(c) and 12(d)], following the complex trajectories shown in Figs. 11(c) and 11(d), a process that due to the aforementioned degeneracy of the first saddle point does not cost any energy.

It is worth noticing that phase locked states with more than two domains (more than two domain walls) never appear in our simulations considering an excitation energy $\Delta K \in [4, 12]$, since already the energy of the second saddle point, $E_{s_1} = 16$, consisting of four domains (four domain walls), is inaccessible. It should be observed, however, for $\Delta K > 16$.

A closer look at Fig. 11 and Fig. 12, particularly a comparison between Fig. 11(b) and Fig. 11(d) [also between Fig. 12(b) and Fig. 12(d)], leads to the conclusion that even a tiny change of the excitation energy ΔK (here only by 0.07%) can lead to a completely different propagation and configuration pattern. We have checked that this is the case also when an infinitesimal perturbation is added to the initial values of the phase space variables ($x_i(0)$, $p_i(0)$). This strong sensitivity to the initial conditions is the hallmark of the chaotic nature of our system in the region of excitation energies $\Delta K > 8$.

As a measure of this sensitivity to the initial conditions in the dipole chain (i.e., its degree of chaoticity), we use the method of the Orthogonal Fast Lyapunov Indicators (OFLIs). In a nutshell, given an m -dimensional flow defined by

$$\frac{d\mathbf{r}}{dt} = \mathbf{f}(\mathbf{r}, t), \quad (27)$$

we examine the time evolution of the variational vector $\delta\mathbf{r}(t)$ given by the (first) variational equations

$$\frac{d\delta\mathbf{r}}{dt} = \frac{\partial \mathbf{f}(\mathbf{r}, t)}{\partial \mathbf{r}} \delta\mathbf{r}. \quad (28)$$

For given initial conditions $\mathbf{r}(0)$ and $\delta\mathbf{r}(0)$, the numerical integration of the systems of differential equations (27) and (28) up to a given final time t_f allows the definition of the OFLI as follows [51–53]:

$$\text{OFLI}(\mathbf{r}(0), \delta\mathbf{r}(0), t_f) = \sup_{0 \leq t \leq t_f} \log \|\delta\mathbf{r}(t)^\perp\|, \quad (29)$$

where \perp indicates the orthogonal component to the flow of the variational vector $\delta\mathbf{r}$. The main advantage of the OFLI is that it provides computationally cheap information about the degree of regularity or chaoticity of a given orbit. In particular, $\delta\mathbf{r}(t)^\perp$ increases linearly with time for regular resonant orbits and

exponentially for chaotic ones [51–53], attaining therefore for long times t_f much larger values for chaotic orbits than the ones for regular orbits. For near-integrable Hamiltonian systems, a rigorous proof of this behavior can be found in Ref. [53]. We note that with the formulation (29), there is a dependence of the value of the OFLI on the initial conditions of the variational vector $\delta\mathbf{r}(0)$. In order to get rid of this dependence we follow the steps found in Refs. [54,55], incorporating also the second order variational equations in the computation of the indicator. For our dipole chain, we have calculated, as a function of the energy excess ΔK , the OFLI for trajectories as those examined so far, featuring initially a single dipole excitation with initial conditions $\mathbf{r}(0) = \{x_k(0) = 0 \forall k, p_{100}(0) = \sqrt{2\Delta K}, p_k(0) = 0 \forall k \neq 100\}$. In our calculations, we stop the computation of the OFLI either when it reaches the cutoff value 9, marking a chaotic trajectory, or when the computation time exceeds our final time $t_f = 5000$, selected empirically according to many numerical simulations.

As an example, we present in Fig. 13(a) the time evolution of the OFLI for two qualitatively different orbits, belonging to the weakly (initial kinetic energy excess $\Delta K = 4$) and to the highly (initial kinetic energy excess $\Delta K = 12$) nonlinear regimes, respectively. We observe in Fig. 13(a) that the OFLI for the $\Delta K = 4$ trajectory increases very slowly, attaining only small values (less than two up to very long times). In contrast the OFLI for the $\Delta K = 12$ trajectory shows a fast increase reaching already at an early stage the cutoff value nine signifying its chaoticity. Note that at our usually selected final simulation time $t_f = 5000$ the distinction between the two trajectories is clear, allowing for their classification as regular ($\Delta K = 4$) and chaotic ($\Delta K = 12$), respectively.

Our results for the behavior of the OFLI as a function of the excess energy ΔK are shown in Fig. 13(b). In the regime $\Delta K \lesssim 6$, the value of the OFLI is below three, indicating the regular behavior of the system in accordance to Fig. 3 and the above discussion. For $6 \lesssim \Delta K \lesssim 8$, the value of the OFLI increases for increasing energy, such that for $\Delta K \gtrsim 8.5$ it becomes larger than the cutoff value 9 characterizing the chaotic orbits. Moreover, the extracted chaoticity of the dipole chain for excitations with energy $\Delta K \gtrsim 8$ provides further evidence for the link of the traveling energy localization patterns shown in Figs. 11(c) and 11(d) and the striking phase locking states associated to them [Figs. 12(c) and 12(d)] to chaotic breathers [16], mentioned above.

As a final remark, it is worth noticing that, in general, the effectiveness of the fast Lyapunov indicators in providing a first indication of the degree of chaoticity of an orbit with a relatively low computational cost has been successfully proven in dynamical systems with few degrees of freedom. Indeed, a global vision of the phase space structure of several Hamiltonian systems with two or three degrees of freedom was obtained by the computation of two-dimensional OFLI maps [54–56]. However, a detailed investigation of the phase space and the chaotic dynamics of multidimensional systems as our dipole chain requires the use of more sophisticated tools based on the computation of Lyapunov exponents [57–59] as deviation vector distributions [60] and Lyapunov weighted dynamics [61,62]. Although very interesting, these investigations go beyond the goal of the present study and will be addressed in a future work.

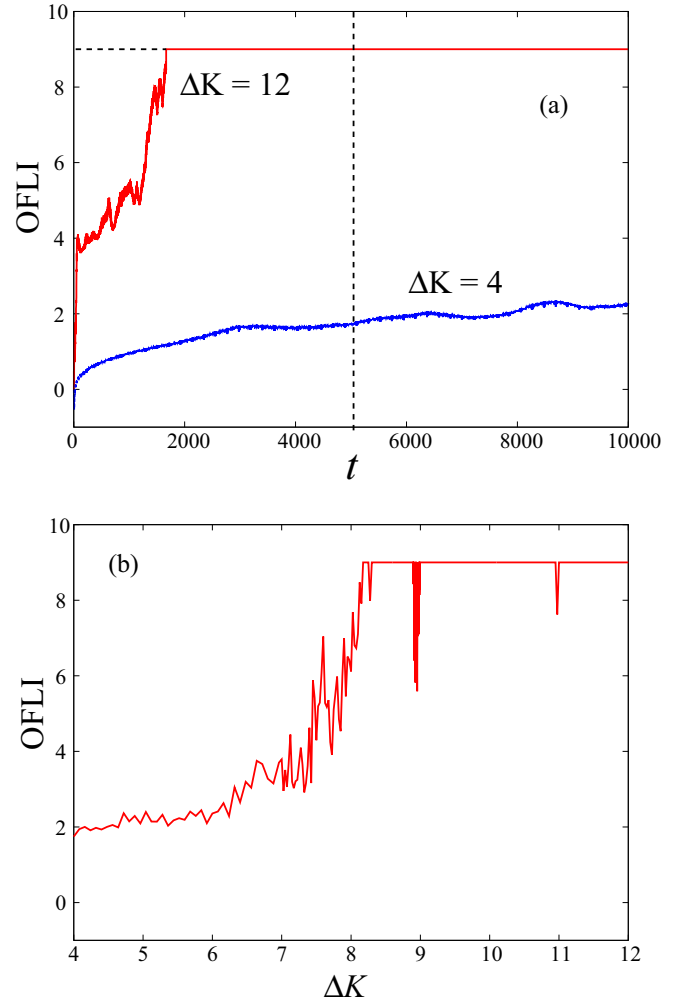


FIG. 13. (a) Time evolution of the OFLI for $\Delta K = 4$ (blue line) and $\Delta K = 12$ (red line). The vertical and horizontal black dashed lines indicate the cutoff value of the OFLI computation and the selected final time $t_f = 5000$ in our simulations, respectively. (b) The OFLI for a dipole chain with a single excited dipole as a function of the excitation energy ΔK . Note that there is a cutoff value of the OFLI for the value 9.

VI. CONCLUSIONS

We have explored the energy transfer mechanisms in a classical dipole chain, modeled as an array of N rigid dipoles with their positions fixed in space, interacting with their NNs and restricted to rotate in a common plane. This leads to a Hamiltonian system of N degrees of freedom describing the rotational dynamics of the dipole chain. The equilibrium points of the equations of motion have been identified and analyzed. It turns out that these can be classified in several families according to their stability, pointing to the high complexity of the potential energy surface of the chain of dipoles. A linearization of the equations of motion around the GS configuration has led to the harmonic approximation of the dipole chain Hamiltonian in terms of normal modes, a fact that has allowed us to extract information about the linear spectrum of the system.

The main focus of this work has been the study of the energy transfer of a localized excitation in the dipole chain for a varying excitation energy. Two regimes with qualitatively different features have been identified. In the first regime of low-energy excitations the system exhibits a weakly nonlinear behavior with the initially localized excitation spreading in the dipole chain, leading for large times to energy equipartition among the dipoles. The second regime of higher energy excitations is characterized by a strong nonlinearity causing energy localization in the form of discrete or chaotic breathers. In some cases the formed chaotic breathers attain the character of domain walls, separating domains of dipoles with different polarization. This spontaneous phase locking of the dipole chain can be linked to the properties of the interaction potential and in particular to its lowest energy saddle point.

It turns out that in the highly nonlinear regime the dipole chain is very sensitive to the initial conditions, indicating its chaotic nature. To quantify the degree of chaoticity in the system for different values of the excitation energy we have calculated the Orthogonal Fast Lyapunov Indicator, which confirms the above discussed picture. For excitation energies below a certain approximate threshold the dynamics is regular whereas above it is highly nonlinear and chaotic. Interestingly enough this threshold energy has a value close to the energy difference between the first saddle and the minimum of the interaction potential.

Suitable experimental realizations of our model could be provided by polar diatomic molecules trapped in a 1D optical lattice [32], colloidal polar particles in optical tweezers [63], or by rotating polar molecules in helium nanodroplets [64]. Further theoretical studies could be devoted to the investigation of the effect of an external homogeneous or inhomogeneous electric field on the dynamics and the energy transfer of a dipole chain as the one studied here. Finally the exploration of the dynamics of the dipole chain in the full $2N$ -dimensional case would also be of interest owing to its even more complex potential landscape.

ACKNOWLEDGMENTS

We thank P. G. Kevrekidis for many useful discussions. J.P.S. acknowledges financial support by the Spanish projects MTM-2014-59433-C2-2-P and MTM2017-88137-C2-2-P (Ministerio de Economía y Competitividad), and the hospitality of the Theory Group of Fundamental Processes in Quantum Physics during his stay at the University of Hamburg.

APPENDIX: THE CHARACTER OF THE CRITICAL POINTS

The nature of the critical points can be judged by the eigenvalues of their Hessian matrix. Due to the NN interactions considered in this study, the Hessian is almost tridiagonal, with an exception regarding the last element of the first row and first element of the last row which are different from zero due to the imposed PBC. In the following we discuss the character of the six families of critical points of the dipole chain based on their Hessian eigenvalues.

1. The minimum E_m and the maximum E_M

The $N \times N$ Hessian matrix of the critical point $\{x_i = 0, \forall i\}$ or $\{x_i = \pi, \forall i\}$ takes the form

$$H_{\min} = \begin{pmatrix} 4 & 1 & 0 & 0 & \cdots & 0 & 1 \\ 1 & 4 & 1 & 0 & \cdots & 0 & 0 \\ 0 & 1 & 4 & 1 & \cdots & 0 & 0 \\ \cdots & \cdots & \cdots & \cdots & \cdots & \cdots & \cdots \\ 0 & 0 & 0 & 0 & \cdots & 4 & 1 \\ 1 & 0 & 0 & 0 & \cdots & 1 & 4 \end{pmatrix}. \quad (\text{A1})$$

If N is large, the last element of the first row and the first element of the last row have a negligible contribution to the eigenspectrum of H_{\min} . Thus, in terms of its eigenspectrum the Hessian can be approximated by the tridiagonal matrix

$$H_{\min} \approx \begin{pmatrix} 4 & 1 & 0 & 0 & \cdots & 0 & 0 \\ 1 & 4 & 1 & 0 & \cdots & 0 & 0 \\ 0 & 1 & 4 & 1 & \cdots & 0 & 0 \\ \cdots & \cdots & \cdots & \cdots & \cdots & \cdots & \cdots \\ 0 & 0 & 0 & 0 & \cdots & 4 & 1 \\ 0 & 0 & 0 & 0 & \cdots & 1 & 4 \end{pmatrix}. \quad (\text{A2})$$

The N eigenvalues of the matrices (A1) and (A2) are real because H_{\min} is symmetric. Moreover, the eigenvalues λ_k of the tridiagonal matrix (A2) are given by [65]

$$\lambda_k = 4 + 2 \cos \frac{k \pi}{(N+1)}.$$

These eigenvalues are positive indicating that also the eigenvalues of the exact matrix (A1) would be positive and in turn that the corresponding critical point is a minimum.

Returning to the original Hessian matrix (A1), the analytic computation of its characteristic equation gives the following polynomial of degree N

$$\begin{aligned} \mathcal{C}_{\text{even}} &\equiv \lambda^N - a_{N-1}\lambda^{N-1} + a_{N-2}\lambda^{N-2} - \cdots - a_1\lambda + a_0 = 0, \\ N &\equiv \text{even}, \end{aligned}$$

$$\begin{aligned} \mathcal{C}_{\text{odd}} &\equiv \lambda^N - a_{N-1}\lambda^{N-1} + a_{N-2}\lambda^{N-2} - \cdots + a_1\lambda - a_0 = 0, \\ N &\equiv \text{odd}, \end{aligned}$$

where $a_i > 0$. This means that there are N sign changes in the sequence of the coefficients $(1, a_{N-1}, a_{N-2}, \dots, a_1, a_0)$. The rule of Descartes [66] says that if p is the number of positive roots of a given polynomial and s is the number of sign changes in the coefficient sequence of this polynomial, then $s = p + 2k$, with k a positive integer. By virtue of this theorem, from the N changes of sign in the coefficients a_i , we conclude that the Hessian (A1) has at most N positive eigenvalues. We can apply the Descartes rule also to extract information about the maximum number of negative roots. Indeed, after replacing $\lambda \rightarrow -\lambda$, the coefficients of the odd degree monomials in λ in the characteristic polynomials $\mathcal{C}_{\text{even,odd}}$ become negative, resulting in no sign changes in the coefficient sequence. This implies that there are no negative eigenvalues and as a consequence all the N eigenvalues of the exact Hessian (A1) are positive.

For the critical point corresponding to the alternating configuration $\{x_i = \pi[1 \pm (-1)^i]/2, \forall i\}$, the Hessian matrix takes the form

$$H_{\max} = -H_{\min}.$$

with approximate eigenvalues

$$\lambda_k = -\left[4 + 2 \cos \frac{k \pi}{(N+1)}\right],$$

which are all negative, indicating that this critical point is a maximum. The analytic computation of the characteristic equation yields

$$\mathcal{C}_{\max} = \lambda^N + a_{N-1}\lambda^{N-1} + a_{N-2}\lambda^{N-2} + \dots + a_1\lambda + a_0 = 0,$$

where $a_i < 0$. Therefore, there are no sign changes in the sequence of the coefficients $(1, a_{N-1}, a_{N-2}, \dots, a_1, a_0)$. In this case, the Descartes rule of signs assures that there are no positive roots of the characteristic polynomial. If we replace $\lambda \rightarrow -\lambda$ in \mathcal{C}_{\max} , the coefficients of the odd degree monomials in λ become negative, a fact that results in N sign changes in the coefficient sequence. Thus the N eigenvalues of H_{\max} are negative and the corresponding critical point is a maximum.

2. The saddle points E_{s1}

For the configurations made of b blocks of n_j dipoles with $x_k = \pi$ while the remaining dipoles possess $x_i = 0$, up to our knowledge, there exists no close expression for the eigenvalues of the corresponding almost tridiagonal Hessian matrix. However, from the numerical computation of the characteristic equation for different values of N and for different number of blocks b , we have strong indications that these critical points are saddle points of rank $2b$ since, by applying the rule of Descartes, we find that the number of positive and negative eigenvalues are $N - 2b$ and $2b$, respectively.

3. The saddle points E_{s2}

For the two configurations $\{x_i = \pi/2, \forall i\}$ or $\{x_i = -\pi/2, \forall i\}$, the Hessian matrix takes the form

$$H_{s3} = \begin{pmatrix} -2 & -2 & 0 & 0 & \dots & 0 & -2 \\ -2 & -2 & -2 & 0 & \dots & 0 & 0 \\ 0 & -2 & -2 & -2 & \dots & 0 & 0 \\ \dots & \dots & \dots & \dots & \dots & \dots & \dots \\ 0 & 0 & 0 & 0 & \dots & -2 & -2 \\ -2 & 0 & 0 & 0 & \dots & -2 & -2 \end{pmatrix}. \quad (\text{A3})$$

Following Ref. [65], the approximate eigenvalues for large N are given by the expression

$$\lambda_k = -2 + 4 \cos \frac{k \pi}{(N+1)}. \quad (\text{A4})$$

From Eq. (A4), we obtain that this critical point is a saddle point with $2(N+1)/3$ hyperbolic directions.

4. The saddle points E_{s3}

For the configuration with alternating angles $\pi/2$ and $-\pi/2$, $\{x_i = \pm(-1)^i \pi/2, \forall i\}$, the Hessian matrix takes the form

$$H_{s3} = \begin{pmatrix} 2 & 2 & 0 & 0 & \dots & 0 & 2 \\ 2 & 2 & 2 & 0 & \dots & 0 & 0 \\ 0 & 2 & 2 & 2 & \dots & 0 & 0 \\ \dots & \dots & \dots & \dots & \dots & \dots & \dots \\ 0 & 0 & 0 & 0 & \dots & 2 & 2 \\ 2 & 0 & 0 & 0 & \dots & 2 & 2 \end{pmatrix}. \quad (\text{A5})$$

Following Ref. [65], the approximate eigenvalues for large N are given by the expression

$$\lambda_k = 2 + 4 \cos \frac{k \pi}{(N+1)}. \quad (\text{A6})$$

From Eq. (A6), we see that this critical point is a saddle point with $(N+1)/3$ hyperbolic directions.

5. The critical points E_{s4}

For the critical points made of all the possible configurations with $x_i = \pm\pi/2$, up to our knowledge, there exists no close expression for the approximate eigenvalues of the corresponding almost tridiagonal Hessian matrix. Moreover, from the numerical computation of the characteristic equation for different configurations, we cannot conclude anything about the nature of these critical points, because, depending on the equilibrium configuration, some of the eigenvalues are zero.

- [1] E. Fermi, J. Pasta, S. Ulam, and M. Tsingou, in *The Many-Body Problem*, edited by D. C. Mattis (World Scientific, Singapore, 1993 reprinted).
- [2] G. P. Berman and F. M. Izrailev, *Chaos* **15**, 015104 (2005).
- [3] T. Dauxois, *Phys. Today* **61**(1), 55 (2008).
- [4] N. J. Zabusky, *Chaos* **15**, 015102 (2005).
- [5] J. Ford, *Phys. Rep.* **213**, 271 (1992).
- [6] G. Gallavotti(ed.), *The Fermi-Pasta-Ulam Problem: A Status Report* (Springer-Verlag, Berlin, 2008).
- [7] A. Mussot, A. Kudlinski, M. Droques, P. Szriftgiser, and N. Akhmediev, *Phys. Rev. X* **4**, 011054 (2014).
- [8] D. Bambusi, A. Carati, A. Maiocchi, and A. Maspero, Some analytic results on the FPU paradox, in *Hamiltonian Partial*

- Differential Equations and Applications*, *Fields Institute Communications*, edited by P. Guyenne, D. Nicholls, and C. Sulem (Springer Science+Business Media, New York, 2015), p. 235.
- [9] T. Penati and S. Flach, *Chaos* **17**, 023102 (2007).
- [10] R. Livi, M. Pettini, S. Ruffo, M. Sparpaglione, and A. Vulpiani, *Phys. Rev. A* **31**, 1039 (1985).
- [11] L. Casetti, M. Cerruti-Sola, M. Pettini, and E. G. D. Cohen, *Phys. Rev. E* **55**, 6566 (1997).
- [12] M. Pettini, L. Casetti, M. Cerruti-Sola, R. Franzosi, and E. G. D. Cohen, *Chaos* **15**, 015106 (2005).
- [13] S. Flach, M. V. Ivanchenko, and O. I. Kanakov, *Phys. Rev. Lett.* **95**, 064102 (2005).
- [14] S. Flach, NOLTA, IEICE **3**, 1 (2015).

- [15] S. Flach and A. V. Gorbach, *Phys. Rep.* **467**, 1 (2008).
- [16] T. Cretegny, T. Dauxois, S. Ruffo, and A. Torcini, *Physica D* **121**, 109 (1998).
- [17] K. Ullmann, A. J. Lichtenberg, and G. Corso, *Phys. Rev. E* **61**, 2471 (2000).
- [18] H. Van Amerongen, L. Valkunas, and R. Van Grondelle, *Photosynthetic Excitons* (World Scientific, Singapore, 2000).
- [19] G. S. Engel, T. R. Calhoun, E. L. Read, T. K. Ahn, T. Mancal, Y. C. Cheng, R. E. Blankenship, and G. R. Fleming, *Nature (London)* **446**, 782 (2007).
- [20] Y.-C. Cheng and G. R. Fleming, *Annu. Rev. Phys. Chem.* **60**, 241 (2009).
- [21] J.I. Wu, F. Liu, J. Ma, R. J. Silbey, and J. Cao, *J. Chem. Phys.* **137**, 174111 (2012).
- [22] I. Burghardt, V. May, D. A. Micha, and E. R. Bittner, *Energy Transfer Dynamics in Biomaterial Systems* (Springer-Verlag, Berlin, 2009).
- [23] S. K. Saikin, A. Eisfeld, S. Valleau, and A. Aspuru-Guzik, *Nanophotonics* **2**, 21 (2013).
- [24] D. Melnikau, D. Savateeva, V. Lesnyak, N. Gaponik, Y. Núñez Fernández, M. I. Vasilevskiy, M. F. Costa, K. E. Mochalov, V. Oleinikov, and Y. P. Rakovich, *Nanoscale* **5**, 9317 (2013).
- [25] Y. Qiao, F. Polzer, H. Kirmse, E. Steeg, S. Kühn, S. Friede, S. Kirstein, and J. P. Rabe, *ACS Nano* **9**, 1552 (2015).
- [26] A. S. Davydov, *Theory of Molecular Excitons* (McGraw-Hill, New York, 1962).
- [27] R. Silbey, *Ann. Rev. Phys. Chem.* **27**, 203 (1976).
- [28] J. D. Wright, *Molecular Crystals*, 2nd ed. (Cambridge University Press, Cambridge, 1994).
- [29] G. S. Kottas, L. I. Clarke, D. Horinek, and J. Michl, *Chem. Rev.* **105**, 1281 (2005).
- [30] R. Krems, B. Friedrich and W. C. Stwalley, *Cold Molecules: Theory, Experiments and Applications* (CRC Press, Boca Raton, FL, 2009).
- [31] M. Weidemüller and C. Zimmermann(eds.), *Cold Atoms and Molecules* (Wiley-VCH, Berlin, 2009).
- [32] T. Lahaye, C. Menotti, L. Santos M. Lewenstein, and T. Pfau, *Rep. Prog. Phys.* **72**, 126401 (2009).
- [33] B. Zhu, J. Schachenmayer, M. Xu, F. H. Urbina, J. G. Restrepo, M. J. Holland, and A. M. Rey, *New J. Phys.* **17**, 083063 (2015).
- [34] T. Sowiński, O. Dutta, P. Hauke, L. Tagliacozzo, and M. Lewenstein, *Phys. Rev. Lett.* **108**, 115301 (2012).
- [35] S. W. DeLeeuw, D. Solvaeson, M. A. Ratner, and J. Michl, *J. Phys. Chem. B* **102**, 3876 (1998).
- [36] E. Sim, M. A. Ratner, and S. W. de Leeuw, *J. Phys. Chem. B* **103**, 8663 (1999).
- [37] J. J. de Jonge, M. A. Ratner, S. W. de Leeuw, and R. O. Simonis, *J. Phys. Chem. B* **108**, 2666 (2004).
- [38] R. González-Férez, M. Iñarrea, J. P. Salas, and P. Schmelcher, *Phys. Rev. E* **95**, 012209 (2017).
- [39] L. Chotorlishvili and J. Berakdar, *J. Phys. B: At. Mol. Opt. Phys.* **40**, 3757 (2007).
- [40] X. Leoncini, A. D. Verga, and S. Ruffo, *Phys. Rev. E* **57**, 6377 (1998).
- [41] M. Cerruti-Sola, C. Clementi, and M. Pettini, *Phys. Rev. E* **61**, 5171 (2000).
- [42] L. Delfini, S. Lepri, and R. Livi, *J. Stat. Mech.* (2005) P05006.
- [43] K. Nam, W.-B. Baek, B. Kim, and S. J. Lee, *J. Stat. Mech.* (2012) P11023.
- [44] P. Noble, *Nonlinearity* **17**, 803 (2004).
- [45] M. Lakshmanan, B. Subash, and A. Saxena, *Phys. Lett. A* **378**, 1119 (2014).
- [46] E. B. Wilson, J. C. Decius, and P. C. Cross, *Molecular Vibrations* (Dover, New York, 1955).
- [47] E. Hairer and G. Wanner, *Solving Ordinary Differential Equations I. Non Stiff Problems* (Springer-Verlag, New York, 1993).
- [48] E. Hairer, C. Lubich, and G. Wanner, *Geometric Numerical Integration. Structure-Preserving Algorithms for Ordinary Differential Equations*, Springer Series in Computational Mathematics 31 (Springer, New York, 2006).
- [49] S. Iubini, O. Boada, Y. Omar, and F. Piazza, *New J. Phys.* **17**, 113030 (2015).
- [50] F. M. Russell, Y. Zolotaryuk, J. C. Eilbeck, and T. Dauxois, *Phys. Rev. B* **55**, 6304 (1997).
- [51] C. Froeschlé and E. Lega, *Celes. Mech. Dyn. Astr.* **78**, 167 (2000).
- [52] M. Fouchard, E. Lega, and C. Froeschlé, *Celes. Mech. Dyn. Astr.* **83**, 205 (2002).
- [53] M. Guzzo, E. Lega, and C. Froeschlé, *Physica D* **163**, 1 (2002).
- [54] R. Barrio, *Chaos Solitons Fractals* **25**, 711 (2005).
- [55] R. Barrio, *Int. J. Bif. Chaos* **16**, 2777 (2006).
- [56] R. González-Férez, M. Iñarrea, J. P. Salas, and P. Schmelcher, *Phys. Rev. E* **90**, 062919 (2014).
- [57] V. I. Oseledets, *Trans. Moscow Math. Soc.* **19**, 197 (1968).
- [58] A. Lichtenberg and M. Leiberman, *Regular and Chaotic Dynamics* (Springer Science, New York, 1992).
- [59] C. Skokos, The Lyapunov characteristic exponents and their computation, in *Dynamics of Small Solar System Bodies and Exoplanets*, Lecture Notes in Physics 790 (Springer-Verlag, Berlin, 2010), pp. 63–135.
- [60] Ch. Skokos, I. Gkolias, and S. Flach, *Phys. Rev. Lett.* **111**, 064101 (2013).
- [61] P. Geiger and C. Dellago, *Chem. Phys.* **375**, 309 (2010).
- [62] T. Laffargue, K.-D. Nguyen Thu Lam, J. Kurchan, and J. Tailleur, *J. Phys. A: Math. Theor.* **46**, 254002 (2013).
- [63] M. Mittal, P. P. Lele, E. W. Kaler, and E. M. Furst, *J. Chem. Phys.* **129**, 064513 (2008).
- [64] B. Shepperson, A. A. Søndergaard, L. Christiansen, J. Kaczmarczyk, R. E. Zillich, M. Lemesko, and H. Stapelfeldt, *Phys. Rev. Lett.* **118**, 203203 (2017).
- [65] W. C. Yueh, *Appl. Math. E-notes* **5**, 66 (2005).
- [66] J. Stoer and R. Bulirsch, *Introduction to Numerical Analysis* (Springer-Verlag, New York, 1983).